Enhanced performance of poly(m-phenylene isophthalamide) (PMIA) composite hollow fiber ultrafiltration membranes by O-MoS$_2$ nanosheets modification

Qinliang Jiang[a,b], Huali Tian[a,b], Kaisong Zhang[a,*]

[a]*Key Laboratory of Urban Pollutant Conversion, Institute of Urban Environment, Chinese Academy of Sciences, Xiamen 361021, China, email: kszhang@iue.ac.cn (K. Zhang)*
[b]*University of Chinese Academy of Sciences, Beijing 10049, China*

ABSTRACT

Poly (m-phenylene isophthalamide) (PMIA) has been widely used for membrane preparation due to its excellent mechanical properties. However, the poor hydrophilicity and inferior antifouling ability has limited its application. To address these problems, the two-dimensional (2D) oxidized molybdenum disulfide (O-MoS$_2$) nanosheets were synthesized as a modifier to fabricate a novel PMIA/O-MoS$_2$ composite hollow fiber ultrafiltration membranes (HFUFMs) by blending O-MoS$_2$ nanosheets in the dope solution. The prepared O-MoS$_2$ nanosheets were subsequently characterized by X-ray diffraction, Raman spectroscopy, thermogravimetric analysis (TGA), energy dispersive spectroscopy, zeta potential. The effects of O-MoS$_2$ nanosheets on membrane properties, including morphology, hydrophilicity, mechanical strength, surface zeta potential, ultrafiltration performance and antifouling characteristics, were also evaluated. The results indicated that the unique properties of O-MoS$_2$ nanosheets endowed the membrane with improved hydrophilicity (contact angle: 55.3° ± 1.2°), electro-negativity (−34.6 ± 2.5 mV, pH = 6.5) and mechanical strength (4.2 ± 0.1 MPa). The composite HFUFMs exhibited enhanced pure water flux (209.0 ± 3.4 L m^{-2} h^{-1} bar^{-1}) and BSA rejection up to 98.0% ± 0.2% which result in a higher flux recovery ratio (90.8% ± 1.5%) than the pristine membrane (60.4% ± 1.2%). This study shows that O-MoS$_2$ nanosheets could be an effective modifier to enhance the performance of PMIA membranes.

Keywords: Enhanced performance; Poly(m-phenylene isophthalamide); Hollow fiber; Ultrafiltration; O-MoS$_2$

1. Introduction

Ultrafiltration (UF), an important membrane technology, has received wide acceptance because of its high efficiency for various treatment applications, such as industrial wastewater treatment, oil–water separation, bio-separation and protein effluent separation [1,2]. Typical engineering materials used to prepare UF membranes are composed of poly(ether sulfone), poly(vinylidene fluoride) and polyacrylonitrile because of their excellent mechanical properties and physical and chemical stabilities [3–5]. Nevertheless, their hydrophobic nature often causes serious membrane fouling during separation processes, and membrane fouling is the major interference limiting universal applications of UF [6]. Poly(m-phenylene isophthalamine) (PMIA), which is one of the most commonly used structural materials for membrane fabrication, has been shown to be an effective material for membrane preparation in the past works [7,8]. Additionally, the fabrication of PMIA membranes by nonsolvent-induced phase separation (NIPS) is quite easy [9], which

* Corresponding author.

is beneficial to the fabrication of large-scale UF membranes [10,11]. However, the poor hydrophilicity and inferior antifouling ability limit their application.

To date, most studies have focused on improving the antifouling performance of membranes by introducing inorganic two-dimensional (2D) nanomaterials. Typical 2D nanomaterials, for example, graphene oxide (GO) nanomaterials and their derivatives, have shown broad application prospects in the field of membrane separation because of their high aspect ratio, low density, good mechanical properties and ability to provide rapid water pathways [12–14]. Based on these advantages, GO nanocomposite membranes have been effectively used to improve water purification. Qin et al. [15] prepared a PVDF nanocomposite membrane by blending a PVDF membrane with GO nanosheets to improve the performance of the blended membrane. Ganesh et al. [16] used GO nanosheets as hydrophilic additives to enhance the permeation performance and salt rejection of relevant polysulfone (PSF) membranes. However, the amphiphilic characteristics of GO inhibit the ability to improve its hydrophilicity (water uptake) on nanocomposite membranes, and because of this, hydrophobic pollutants (proteins) could be deposited on the hybrid membrane surface.

Newly developed 2D nanomaterials such as MoS_2 [17–20], C_3N_4 [21,22], WS_2 [23] and h-boron nitride (BN) [24] nanosheets may have potential application prospects for the separation and purification of water. MoS_2 is a graphene-like 2D nanolayered compound [25], with broad application prospects for molecular separation [26]. The S/Mo atoms in MoS_2 nanosheets exhibit high negative charge properties and hydrophilic sites, and many researchers have used MoS_2 nanomaterials to modify the physical and chemical properties, including roughness and zeta potential, of membrane surfaces to improve the membrane permeability and antifouling [19]. Moreover, adding MoS_2 nanosheets into a polymer to prepare UF membranes has become a research focus to control the pore structure of UF membranes [27]. Pan et al. [28] used MoS_2 nanosheets to construct a transmission pathway in a hybrid membrane. Xu et al. [20] added novel amphoteric ion-functionalized MoS_2 nanosheets to fabricate a composite membrane for salt/dye separation. However, the dispersion of two-dimensional MoS_2 nanosheets in aqueous or organic solvent is still a challenge when using as a filler in membrane due to their high surface energy, which restricts the well distribution of nanosheets on membrane surface or polymer matrix. Li et al. [19] found that the existed aggregation of exfoliated MoS_2 nanosheets on polyamide matrix hindered the further enhancement of separation performances of nanocomposite membrane. Thus, there is a critical need to improve the compatibility between inorganic nanomaterial and polymer matrix so as to maximize the special functionalities of 2D nanomaterials.

GO, has oxygen-containing functional groups (oxygen atoms and hydrogen atoms) on the edges and surface of its nanosheets, making it a potential candidate material on account of its unique 2D layer structure and great dispersibility [29]. Though, GO can be combined with polymers to enhance the membrane performance, but this method is relatively expensive. Molybdenum disulfide oxide (O-MoS_2), which has a two-dimensional structure similar to that of GO,

is expected to be a new alternative material for GO and has never been explored for the preparation of PMIA composite hollow fiber ultrafiltration membranes (HFUFMs).

In this study, MoS_2 will be further functionalized by acid treatment, oxidization and ultrasonication to prepare a highly hydrophilic modifier, O-MoS_2, to enhance the permeability and antifouling ability of a membrane without sacrificing selectivity. In addition, the high surface area of O-MoS_2 and its negatively charged groups in the membrane separation layer are conducive to maintaining pollutant exclusion and providing additional pathways for water seepage. To achieve this objective, O-MoS_2 was synthesized and added as a modifier to fabricate PMIA/O-MoS_2 composite HFUFMs. The properties of membranes with different O-MoS_2 concentrations were determined. In addition to the morphological and chemical characterizations of the membranes, their antifouling performance was investigated with a humic acid (HA) solution, and the membranes were also used to remove bovine serum albumin (BSA) and HA from an aqueous solution.

2. Experimental

2.1. Materials

PMIA was supplied by DuPont Company. MoS_2 was purchased from Sigma-Aldrich (Germany). LiCl was purchased from Sinopharm Chemical Reagent Co., Ltd. (Shanghai, China). N,N-Dimethylacetamide (DMAc was supplied by Shanghai Jingwei Chemical Co. Ltd.). Polyethylene glycol (PEG), BSA (Mw = 67,000) and HA were purchased from Sigma-Aldrich (Germany). All other experimental reagents were supplied from Sinopharm Chemical Reagent Co.

2.2. Synthesis of O-MoS_2

O-MoS_2 nanosheets were synthesized from pristine MoS_2 powder by a process modified from that reported in previous literature [30]. The specific process is as follows: 3.0 g MoS_2 powder and 1.0 g $NaNO_3$ were placed into a 500 mL beaker. Then, 50 mL 98 wt.% H_2SO_4 was added dropwise to the powder mixture and followed by slow addition of 6.0 g $KMnO_4$ at 0°C. Then, the mixture was transferred to an oil bath (35°C) and rapidly mixed for 3 h. After mixing, 50 mL deionized water (DI) water was carefully added, and the mixture was stirred at 0°C for approximately 30 min. After that, the mixture was allowed to warm up in ambient air for 30 min before another 100 mL DI water was added. Subsequently, 8.0 mL of 30% H_2O_2 was added. The final product was filtered and dried under vacuum. Finally, various concentrations of O-MoS_2 were blended in a DMAc, and the mixture was ultrasonicated at 500 watts for 2 h.

2.3. Membrane preparation

The casting solution was obtained by dissolving a certain concentration of PMIA and additives in solvent under stirring at 60°C until a uniform PMIA solution was prepared. Then, the solution was kept in a 5-L reaction tank (50°C, 8 h) for vacuum degassing. Table 1 lists the information for all prepared solutions.

Table 1
Spinning parameters for samples M0-M4

Membrane No.	PMIA (wt.%)	LiCl (wt.%)	PEG (wt.%)	O-MoS$_2$ (wt.%)	DMAc (wt.%)	Viscosity (cp)
M0	14	4	3	0	79.0	4,860 ± 22
M1	14	4	3	0.1	78.9	5,180 ± 20
M2	14	4	3	0.2	78.8	5,300 ± 16
M3	14	4	3	0.25	78.75	5,360 ± 20
M4	14	4	3	0.3	78.7	5,380 ± 18

As shown in Fig. 1, during the dry-wet phase inversion process of the PMIA hollow fiber UF membranes, the polymer solution was co-extruded with a bore fluid (tap water) by an accurate syringe pump to adjust the doping flow rate. The extruded solution was exposed to air and subsequently placed in an external coagulant bath (tap water). The detailed parameters of the spinning process are listed in Table 2. The membranes were immersed in a tap water bath for at least 24 h to remove residual DMAc and additives. Finally, the fibers were placed into a 3/7 glycerol/water solution for 24 h prior to air drying.

2.4. Characterization

2.4.1. Characterization of MoS$_2$ and O-MoS$_2$

Raman spectroscopy and X-ray diffraction (XRD) analyses were conducted for chemical and crystalline analyses of MoS$_2$ and O-MoS$_2$. Their thermal stability was analysed with a Netzsch TG 209 F3 TGA system. The elemental distribution of MoS$_2$ and O-MoS$_2$ was obtained by energy dispersive spectroscopy (EDS) (HITACHI S4800, Hitachi, Ltd.).

2.4.2. Viscosity

The viscosity of the dopant was measured with a spindle of S64 by a numerical display viscometer (LVDC-C, Brookfield, United States) at room temperature.

Table 2
Preparation parameters and spinning conditions of the HFMs

Preparation parameters/spinning conditions	Value
Dope solution temperature (°C)	50.0
Spinneret dimension OD/ID (mm/mm)	1.6/0.9
Dope solution flow rate (mL/min)	5.7
Bore solution flow rate (mL/min)	4.7
Bore solution	Deionized water
External coagulation	Tap water
Coagulation temperature (°C)	25 ± 1.0
Air gap distance (cm)	10.0
Take up speed	Free fall

2.4.3. Characterization of the membranes

The morphology of the PMIA HFMs was observed by field emission scanning electron microscopy (FESEM, HITACHI S4800, Hitachi, Ltd.). The top surfaces of the samples were examined by atomic force microscopy (AFM, Agilent Technologies-5500). Hydrophilicity of the resultant membranes was comparatively analysed with contact angle (CA, KRUSS DSA30, Germany). The surface zeta potential of the membranes was measured by streaming potential measurements with a SurPASS electrokinetic analyser (SurPASS, Anton Paar GmbH). The mechanical strength
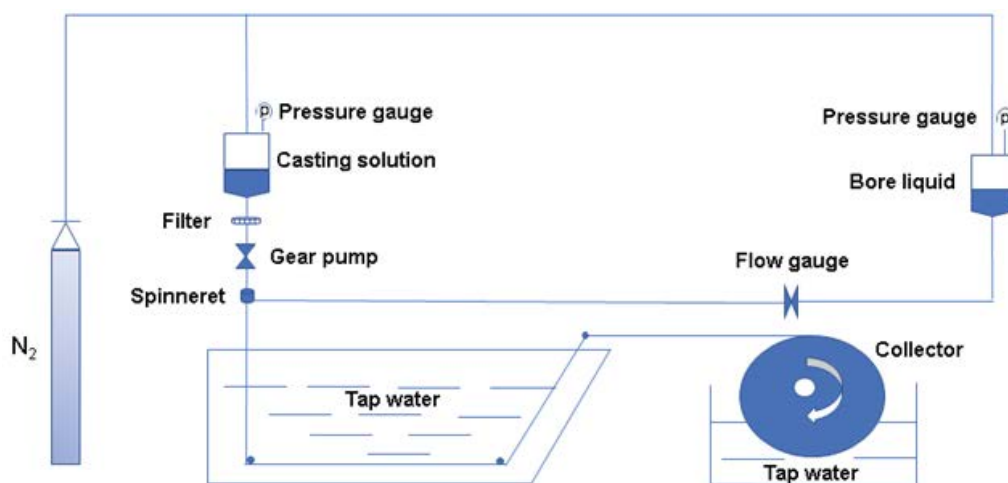
Fig. 1. Schematic diagram of the spinning apparatus for PMIA HFUFMs.

of the membranes was tested by tensile testing equipment (INSTRON-5565). The zeta potential of MoS_2 and O-MoS_2 was tested by using a Zetasizer 3000 HSA (Malvern Instruments) under the condition that 0.25 mg MoS_2 and O-MoS_2 nanosheets were dispersed in 1 mL deionized water at different pH values, respectively.

2.4.4. Porosity, pore size and distribution

The membrane porosity ε (%) was defined as the volume of the membrane pores divided by the total volume of the membranes and can be calculated by a gravimetric method [31]:

$$\varepsilon\left(\%\right) = \frac{(W1 - W2)/\rho_w}{(W1 - W2)/\rho_w + (W2/\rho_p)} \times 100\%$$ (1)

where W_1 is the weight of the wet membrane (g), W_2 is the weight of the dry membrane (g), ρ_p and ρ_w are the density of the polymer and water, respectively. All samples were tested five times, and the average value was taken.

The pore size and its distribution data of the membrane surface were kindly offered by Nanjing Tech University with a membrane pore analyser (PSMA-10, XuH Science and Technology Co. Ltd., China) based on liquid/liquid displacement porosimetry as described in previous researches [32–34].

2.4.5. Ultrafiltration experiments

A self-prepared membrane module was used in the pure water permeation flux (PWF) and BSA and HA rejection tests and two fibers (effective length ~44 cm) were fixed for each test. The PWF of the resultant membrane was measured by a cross-flow UF system with DI water (pre-pressurized at 0.15 MPa for 30 min with DI water). All experiments were carried out at a constant temperature (25°C ± 1°C) and 0.10 MPa. Then, the rejection tests of samples were performed with 10, 50, 100, 500 ppm HA (pH = 6.8) and 1,000 ppm BSA solutions (pH = 7.4). The permeation flux and rejection of the membranes were measured and calculated by Eqs. (2)–(4) [35].

$$J_{w1} = \frac{Q}{A \times t}$$ (2)

$$RHA = \left(1 - \frac{C_p}{C_f}\right)$$ (3)

$$RBSA = \left(1 - \frac{C_p}{C_f}\right)$$ (4)

where J_{w1} is the PWF in L m^{-2} h^{-1} bar^{-1}, Q is the volume of the membrane permeate in L, t is the testing time in h and A is the effective membrane area in m^2. RHA and RBSA are the HA and BSA rejection rates of the membrane, and C_p and C_f are the solute concentrations of permeate and feed, respectively, in mg L^{-1}.

2.4.6. Antifouling and cleaning efficiency tests

To further confirm the antifouling ability of the composite HFUFMs, ultrafiltration regeneration experiments were carried out using membranes M0, M2 and M4. A 500 ppm HA solution was used in the antifouling tests. First, the prepared membrane was continuously operated in a HA solution for 100 min under a pressure of 0.1 MPa. Second, the samples were cleaned with DI water for 0.5 h. Third, the permeation flux of the rinsed membrane was re-tested, denoted as J_{W2}. The above three processes were performed for five cycles. The calculation of the total fouling (Rt), reversible fouling (Rr), irreversible fouling (Rir) and flux recovery ratio (FRR) was performed by Eqs. (5)–(8):

$$Rt\left(\%\right) = \left(1 - \frac{J_W}{J_{W1}}\right) \times 100\%$$ (5)

$$Rr\left(\%\right) = \left(\frac{J_{W2} - J_W}{J_W}\right) \times 100\%$$ (6)

$$Rir = \left(\frac{J_{W1} - J_{W2}}{J_{W1}}\right) \times 100\%$$ (7)

$$FRR = \frac{J_{W2}}{J_{W1}} \times 100\%$$ (8)

where J_W is the flux of the HA solution.

3. Results and discussion

3.1. Characterization of O-MoS_2

TEM images of MoS_2 and O-MoS_2 at different magnifications are presented in Fig. 2. As can be seen from Fig. 2a, the pristine MoS_2 had a large size, thick, regular boundary and layer structure, similar to blade-shaped, it showed graphite black color as a whole. Compared with MoS_2, O-MoS_2 is smaller in size, thinner, with irregular bedded edges, similar to gear structure and lighter color than MoS_2. This gear structure means a small amount of single layer O-MoS_2 peel off and the edge and size change may be caused by MoS_2 being oxidized.

To analyse the chemical change in MoS_2 before and after oxidation, Raman, XRD, thermogravimetric analyses and contact angle were conducted. As shown in Fig. 3a, the A_{1g} (out of plane) and in-plane E_{2g}^1 bands of MoS_2 were detected at 382 cm^{-1} in the Raman spectra of both the MoS_2 and O-MoS_2 samples, and these bands can be ascribed to Mo-S vibrations [36]. The peaks at 406 cm^{-1} were assigned to the out-of-plane vibrations (A_{1g} mode) of the two samples [37]. However, the bond strength of O-MoS_2 slightly changed. The intensity ratio between the A_{1g} and E_{2g}^1 modes (A_{1g}/E_{2g}^1) decreased from 1.9 to 1.0. The changes in the peak intensity may be due to the appearance of new oxygen-containing groups. Fig. 3b shows the normalized XRD spectra of MoS_2 before and after oxidation. The characteristic peaks at 14.4°, 32.7°, 39.6°, 49.8° and 58.0° correspond to the typical (002), (100), (103), (105)
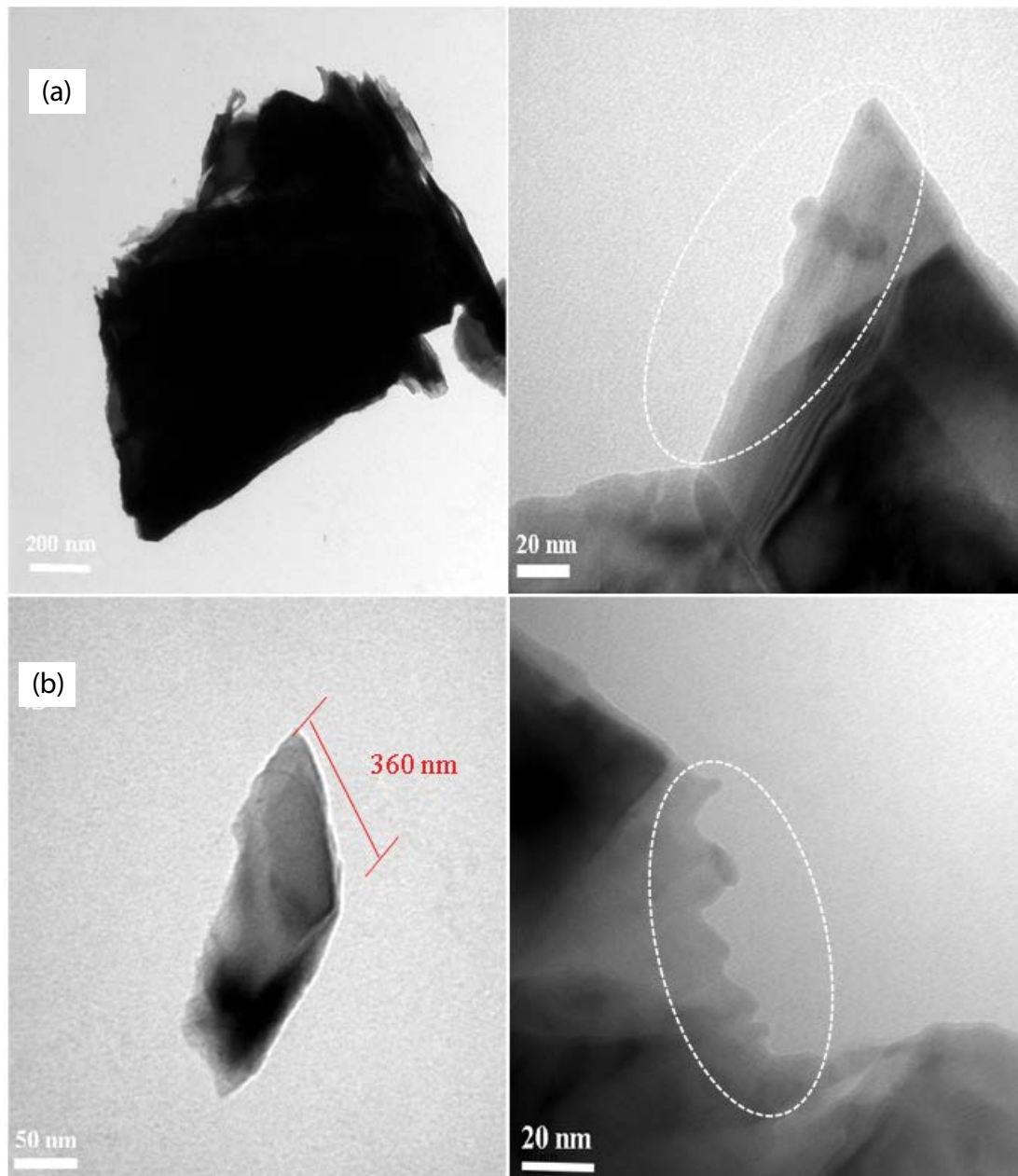
Fig. 2. TEM image of (a) pristine MoS_2 and (b) O-MoS_2.

and (110) crystal planes of the MoS_2 nanosheets, respectively [38]. It should be noticed that the intensity of these peaks in O-MoS_2 XRD pattern significantly decreased due to its more loose structure and higher exfoliation comparing with that of the pristine MoS_2 [30].

The thermograms of MoS_2 and oxidized MoS_2 were obtained, and the curves are presented in Fig. 3c. A lower mass loss was observed for MoS_2 than O-MoS_2 due to degradation of the additional oxygen-containing groups in O-MoS_2. These results further proved that oxygen-containing groups existed in O-MoS_2, as mentioned in the above tests. The results are also shown in Fig. 3d, indicating that MoS_2 and O-MoS_2 have a high negative charge when dispersed in DI water at different pH values. In the pH range of 3–10, the

zeta negative potential of O-MoS_2 nanosheet is greater than that of the bulk MoS_2, demonstrating that there are more sulfur edge sites on the O-MoS_2 nanosheet. As shown in Fig. 3e, the contact angle of pristine MoS_2 (85.7°), revealed a weak surface hydrophilicity of original MoS_2 nanosheet. However, the hydrophilicity of O-MoS_2 nanosheets significantly improved (contact angle decreased from 85.7° to 40.5°).

EDS was conducted for further quantitative analysis of MoS_2 oxidation, and the results are shown in Fig. 4. It shows that only O, S and Mo were detected for the samples both before and after oxidation. The increased weight (%) and atomic (%) of O indicated the successful oxidation of MoS_2. It is worth mentioning that O was also detected in MoS_2 before oxidation, which was believed to be due to trace of impurities.
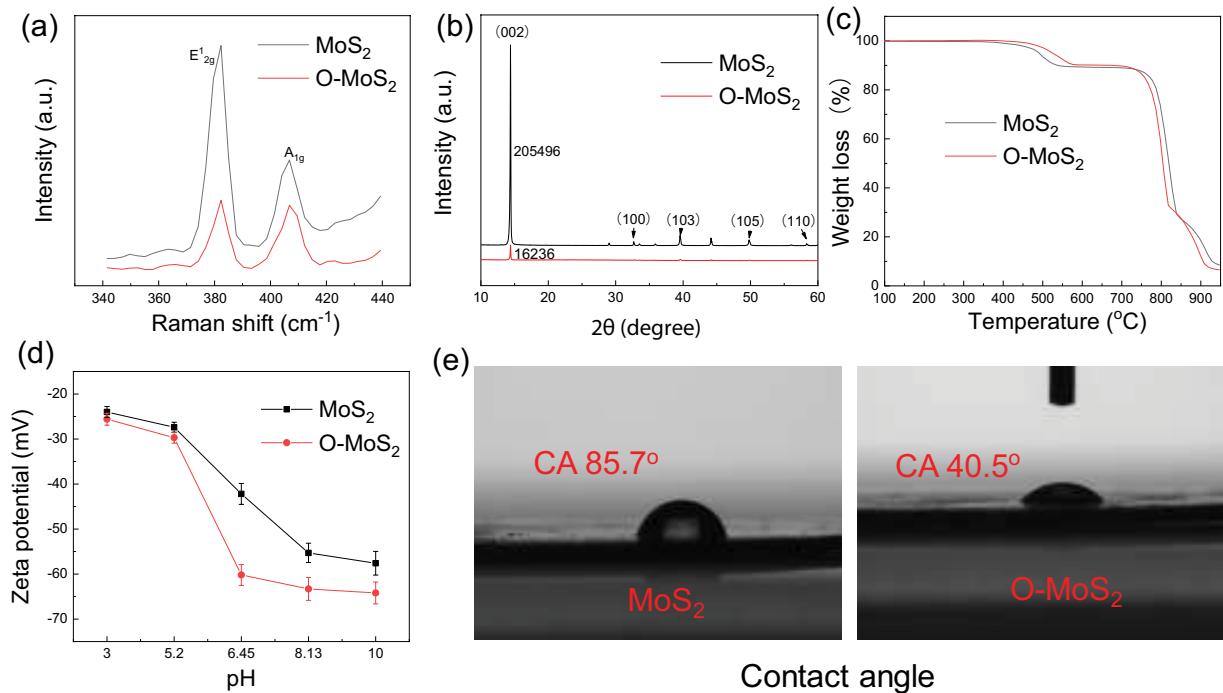
Fig. 3. Analysis of pristine MoS_2 and oxidized MoS_2 (a) Raman, (b) X-ray diffractograms, (c) thermogravimetric analysis, (d) zeta potential in water with different pH values and (e) contact angle, respectively.
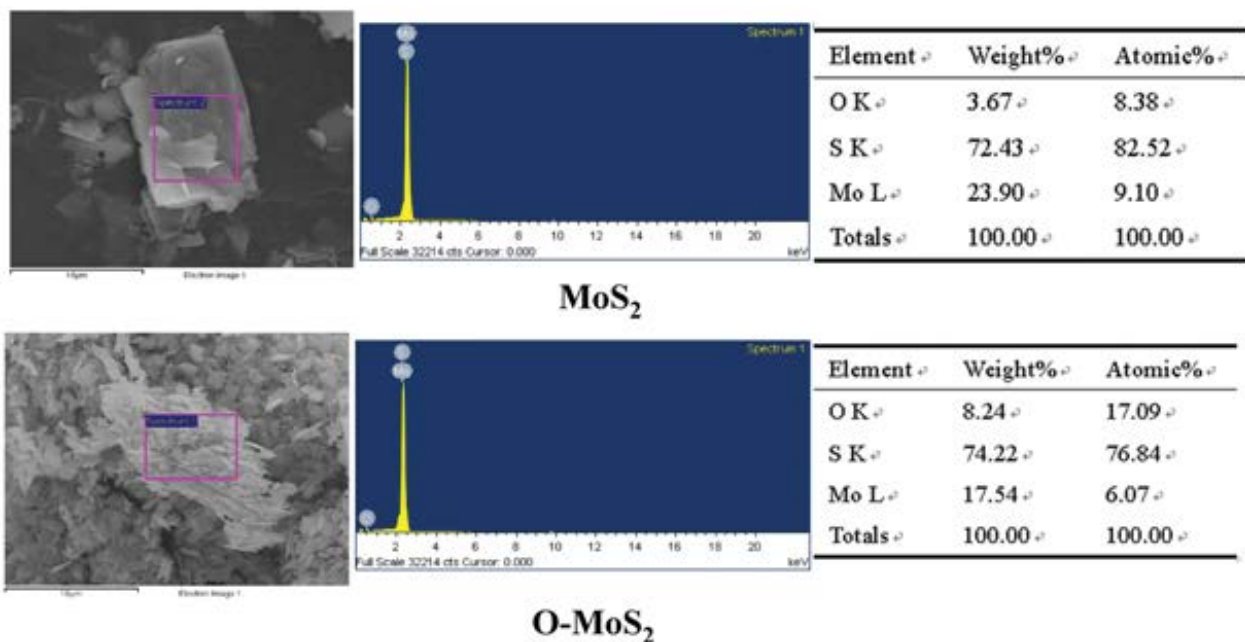
Fig. 4. EDS analysis of MoS_2 and $O\text{-}MoS_2$.

The increase in the O content of MoS_2 enhances its partial oxidation following the oxidation reaction mentioned above.

3.2. Characterization of the membranes

Figs. 5a1–e1 show that all of the studied membranes have similar asymmetrical cross-section structures with a selective ultra-thin skin layer on top of macro-voids and finger-like sublayers. However, an obvious nanosheet-like structure (Figs. 5b1–e1) can be observed in the cross-section of the $O\text{-}MoS_2$ composite HFUFMs, and this structure is different from that of the pristine membrane shown in Fig. 5a1. At the same time, the large macro-voids in the inner layer of the pristine membrane were replaced by a sponge-like structure
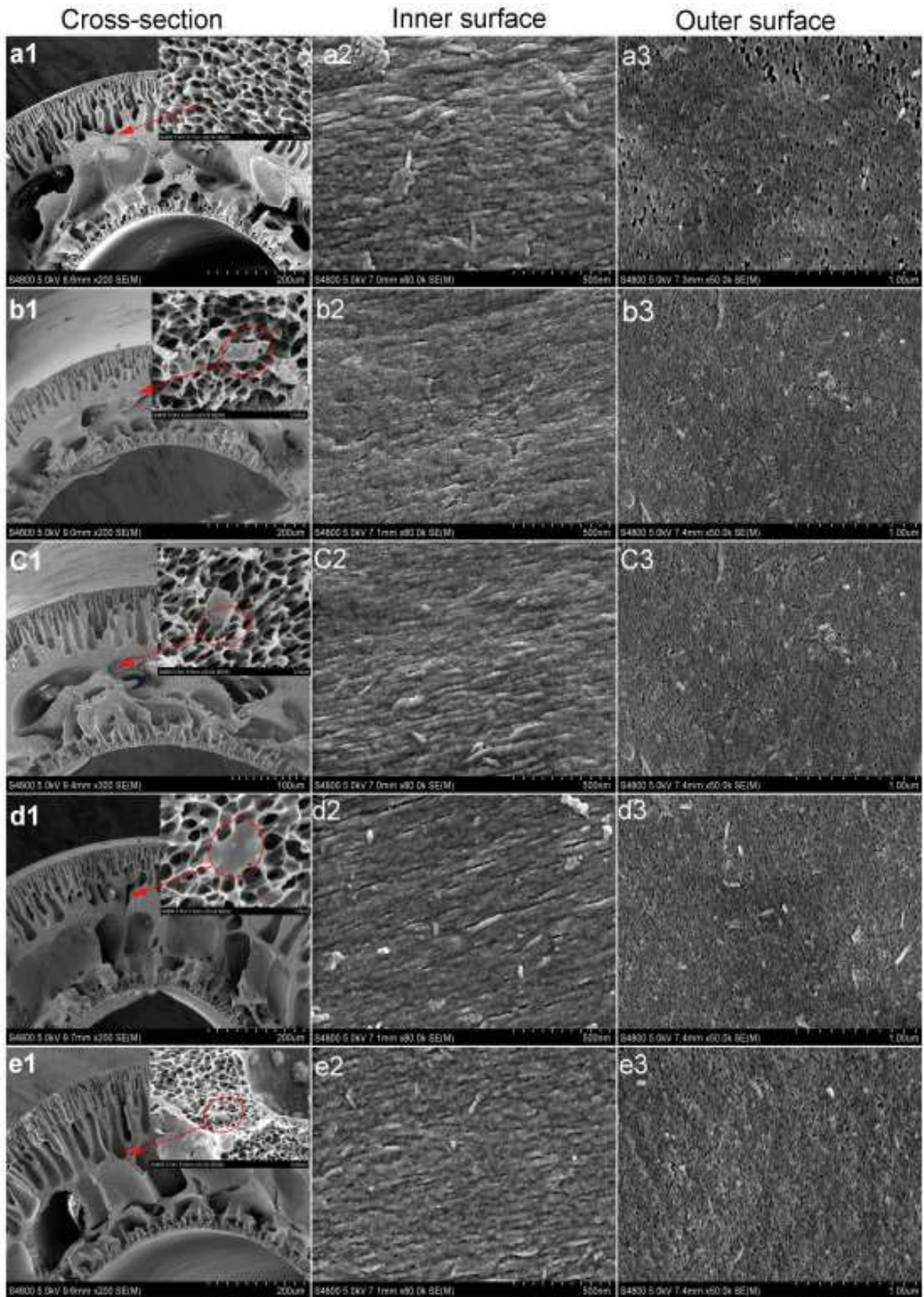
Fig. 5. SEM cross-sectional, inner and outer surface images for (a1–a3) M0, (b1–b3) M1, (c1–c3) M2, (d1–d3) M3, (e1–e3) M4.

after O-MoS$_2$ was added at a content below 0.20 wt.%, and this change caused both the number of pores and pore size under the skin layer of the modified membranes to decrease. This structural change might be due to the increase in the doping viscosity (from 4,860 to 5,300 cp) with the content of O-MoS$_2$ in the doping solution increasing from 0 to 0.2 wt.%. A high viscosity polymer solution would slow down the diffusion of nonsolvent into membranes, which would decrease the exchange speeds between the solvent solution and water and suppress the formation of large macro-voids. However, a higher O-MoS$_2$ content (more than 0.2 wt.%) in a membrane creates finger-like macro-voids that are wider than the sponge-like structures, as shown in Figs. 5d1 and e1. This difference can be attributed to thermodynamic and kinetic changes when O-MoS$_2$ with a content higher than 0.20 wt.% was used [3]. The addition of hydrophilic O-MoS$_2$ nanosheets can facilitate the diffusion rate of DMAc/water and lead to a thinner sponge-like structure that occupies the middle section of the membrane and cover larger macro-voids.

In addition to the cross-sectional morphologies, the morphologies of the inner and outer surfaces of the modified HFUFMs and their FESEM images are shown in Figs. 5b2–e2 and Figs. 5b3–e3. Dense inner (Figs. 5b2–e2) and outer surfaces (Figs. 5b3–e3) without any macroscopic defects can be observed. This phenomenon shows that the good dispersion of O-MoS$_2$ in the PMIA casting solution was confirmed by the lack of obvious defects or O-MoS$_2$ aggregation on the inner and outer surfaces.

The addition of O-MoS$_2$ can also affect membrane surface roughness, which is an important factor influencing the permeability and antifouling ability of membranes. AFM was used to determine the outer surface roughness, and the results are shown in Fig. 6. In the figure, the 3D AFM images of the tested membranes are shown with a top surface scan size of 2 μm × 2 μm. It is obvious that the surfaces of all the hybrid membranes are much rougher than those of the pure membranes. The roughness test results shown in Table 3 quantitatively confirm the AFM results.

The surface roughness of the membrane samples showed a positive relationship with the addition of oxidized MoS$_2$ when its content was below 0.25 wt.%. However, further increase in the O-MoS$_2$ concentration (≥0.25 wt.%) had a negative relationship with the membrane roughness. The composite membrane with 0.25 wt.% O-MoS$_2$ had the highest surface roughness value of 25.3 nm, which was a nearly 300% increase in roughness compared with that of the pristine membrane. A membrane with a higher surface roughness has a higher surface area, which is desirable for promoting permeability [39]. Generally, a high surface roughness would result in poor antifouling properties for a hydrophobic

Table 3
Detailed surface data of pristine PMIA and PMIA/O-MoS$_2$ HFMs

Membrane No.	Ra (nm)	Rq (nm)	Rz (nm)
M0	8.4	11.9	111.0
M1	21.1	28.4	220.0
M2	20.5	28.9	375.0
M3	25.2	33.8	302.0
M4	20.9	27.5	248.0
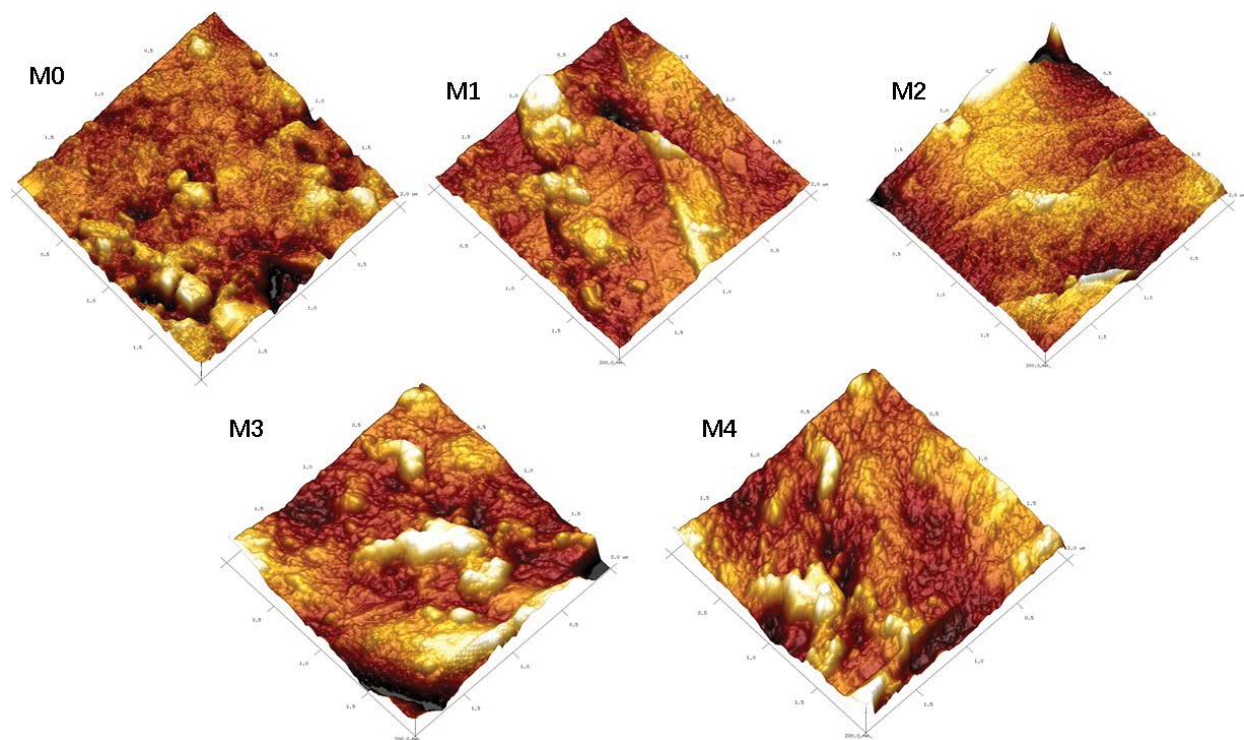
Fig. 6. AFM images of the outer surfaces of pristine membrane (M0) and composite HFUFMs with different O-MoS$_2$ contents. (M1) 0.10 wt.% O-MoS$_2$, (M2) 0.20 wt.% O-MoS$_2$, (M3) 0.25 wt.% O-MoS$_2$, (M4) 0.30 wt.% O-MoS$_2$.

membrane but enhanced antifouling properties for a hydrophilic surface [14].

The contact angle indicates hydrophilicity, that is, a lower water contact angle indicates a greater hydrophilicity and a higher angle indicates lower hydrophilicity, and is related to the antifouling ability and permeability of membranes [40]. As shown in Fig. 7a, the contact angles of all O-MoS$_2$ composite HFUFMs decreased relative to the contact angle of the original membrane, and the decrease positively correlated with the O-MoS$_2$ content, which indicated a hydrophilicity improvement of the tested membranes. The CA was the lowest (55.3°) when 0.30 wt.% O-MoS$_2$ (highest content added in this work) was doped into the membrane, illustrating the higher hydrophilicity of this membranes compared with that of the pristine ones (72.9°). The improvement in the hydrophilicity by adding O-MoS$_2$ is attributed to the hydrophilic nature of O-MoS$_2$ (Fig. 3e) and its effects during the membrane fabrication process. A higher concentration of O-MoS$_2$ in the casting solution migrated to the membrane surface and increased its surface concentration, allowing

more water interactions on the membrane surface (O–H and oxygen-containing groups) due to the presence of hydrophilic O-MoS$_2$ and resulting in a higher hydrophilicity. At the same time, the hydrophilicity enhancement by O-MoS$_2$ can promote the exchange rate between DMAc and water in the phase-inversion process when the doping amount is less than 0.25 wt.%, as mentioned above.

The surface electrical properties of composite HFUFMs can be changed by adding O-MoS$_2$ nanosheets. Fig. 7b shows the zeta potential value of the membranes in terms of pH value. The surface zeta potential of the pristine membrane was positive at pH = 3 whereas a negative value (–11.7 mV) was obtained at pH = 4. This was attributed to the adsorption of hydroxyl groups on the unfunctionalized PMIA HFUFMs from the aqueous solution [41]. The composite membranes were negatively charged in the pH range between 3 and 10. In addition, the zeta potential values of the O-MoS$_2$ hybrid membranes were more negative than those of the pristine membranes (Fig. 7b). The absolute zeta potential values of the composite membranes increased with the addition of
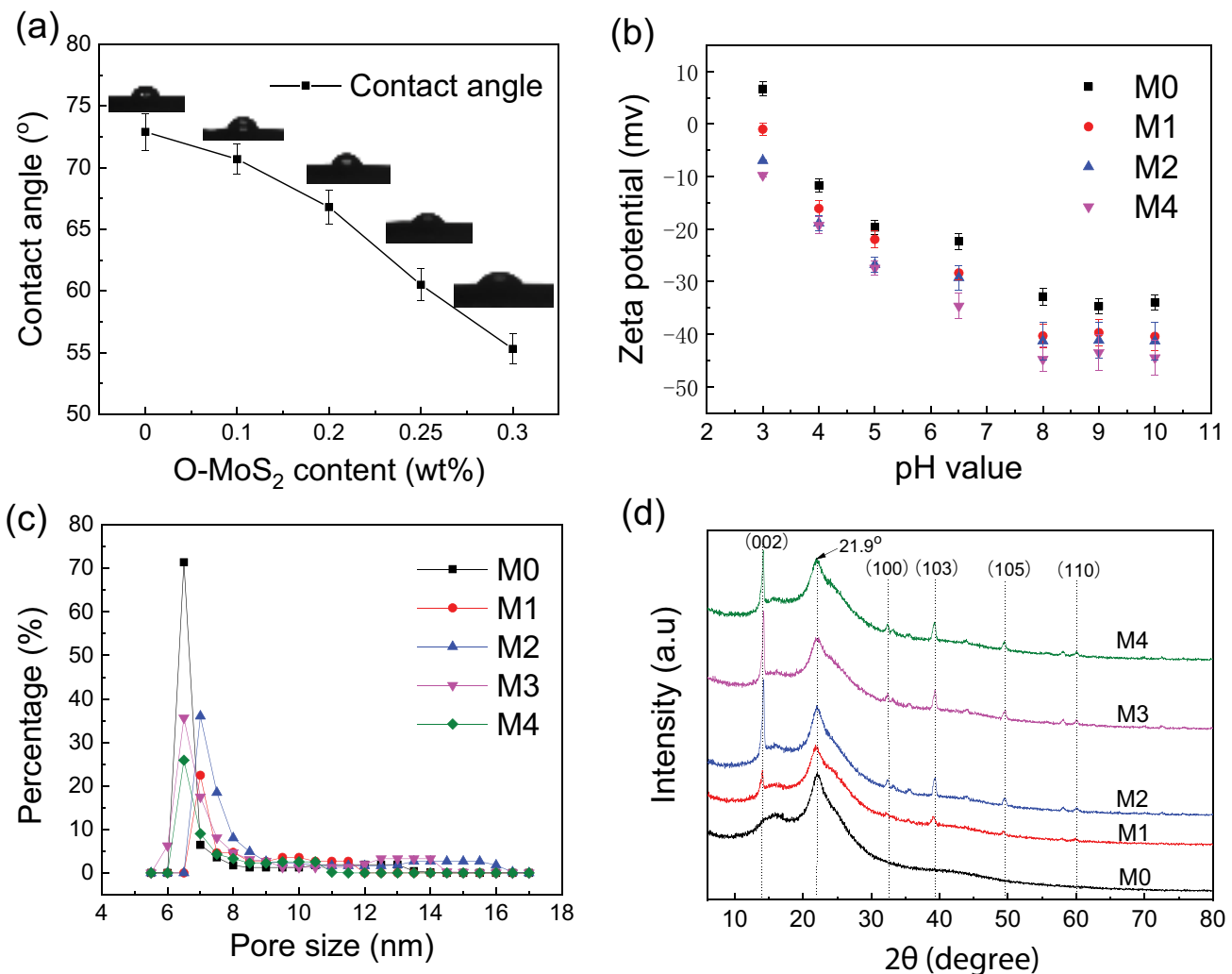
Fig. 7. Analysis of pristine PMIA and PMIA/O-MoS$_2$ HFUFMs (a) contact angles, (b) zeta potential in terms of pH value, (c) pore size distribution and (d) XRD patterns, respectively.

O-MoS$_2$, which proved the successful loading of highly negatively charged O-MoS$_2$ on the membrane surfaces (Fig. 3d) [42]. A negatively charged membrane surface has a positive effect on the antifouling ability of negatively charged contaminants (e.g., BSA and HA). At the same time, Fig. 7c presents that mean pore size (d_p) value first increases from 6.5 nm for M0 to 7.8 nm for M2 and cuts back slightly to 7.0 nm for M4. It is well known that pore size has a great effect on the permeation flux of the membrane [43], meanwhile the resultant membrane pore size with most pores in the range of 10–20 nm, implying that membranes with great UF performances were obtained.

The XRD patterns of O-MoS$_2$/PMIA membranes with various O-MoS$_2$ contents are presented in Fig. 7d. Both of the pure PMIA and O-MoS$_2$/PMIA HFUFMs had a prominent diffraction peak at 2θ = 21.9°, and the differences in this peak were very small, which is similar to the results shown in Fig. 3d; that is, the addition of O-MoS$_2$ has little influence on the crystallinity of PMIA fibers. In addition, it indicates that patterns of the composite membranes had five peaks for (002), (100), (103), (105) and (110) reflections, which are characteristic of crystalline O-MoS$_2$ (Fig. 3b), and these peaks proved that the O-MoS$_2$ nanosheets were loaded in the composite HFUFMs. Moreover, it also shows that the intensity of these peaks in XRD pattern increased significantly, and the increase of these peak strengths implies that more O-MoS$_2$ nanosheets were loaded on the surface of the composite membrane.

The mechanical properties of the resultant membranes, that is, break strength, elongation at break, and Young's modulus, are shown in Table 4. It shows that the tensile strengths of composite HFUFMs increased (from 3.8 to 4.3 MPa) with the addition of O-MoS$_2$ when the O-MoS$_2$ content was 0.25 wt.%. The same increasing trend occurred for the Young's modulus values of M0 and M3, which increased from 162.8 to 183.4 MPa, respectively. This change is due to the excellent compatibility of O-MoS$_2$ with PMIA, which allows the polymer matrix to be endowed with the excellent mechanical properties of O-MoS$_2$ and results in a much higher tensile strength (4.3 MPa) and Young's modulus (183.4 MPa) for the M3 membrane than M0 membrane. However, as the further increase of O-MoS$_2$ content, the tensile strength and Young's modulus of the M4 membrane were lower than those of the M3 membrane, which is due to the aggregation of large O-MoS$_2$ nanosheets when the concentration of O-MoS$_2$ increased [44].

Table 4
Mechanical properties of pristine PMIA and PMIA/O-MoS$_2$ HFMs

Membrane no.	Tensile strength (MPa)	Breaking elongation (%)	Yang's modulus (MPa)
M0	3.8 ± 0.1	63.0 ± 3.4	162.8 ± 2.1
M1	4.1 ± 0.2	62.7 ± 5.5	174.3 ± 3.7
M2	4.2 ± 0.1	60.5 ± 4.6	178.9 ± 4.3
M3	4.3 ± 0.3	56.5 ± 3.2	183.4 ± 3.6
M4	3.9 ± 0.2	71.2 ± 7.0	179.1 ± 3.4

3.3. Permeability

Fig. 8 shows the performance of the membranes before and after the addition of O-MoS$_2$. The BSA rejection rates of all the modified membranes were higher than that of the pristine PMIA membrane. This result was due to the enhanced hydrophilicity and surface negative charge of the composite membranes upon the addition of O-MoS$_2$. The increase of negative charge on the surface of composite HFUFMs was due to the presence of the O-MoS$_2$, which provided higher protein rejections by electrostatic repulsion interaction between composite HFUFMs surface and negatively charged BSA protein [45].

The pure water flux of the composite HFUFMs increased with the O-MoS$_2$ content and reached the highest value when the content of O-MoS$_2$ was 0.20 wt.%. The continuous increase (from 158.3 to 209.0 L m^{-2} h^{-1} bar^{-1}) in the PWF of the composite membranes can be attributed to (i) the decrease in the water contact angle with the O-MoS$_2$ contents increase from 0.0 to 0.20 wt.%, which improves the hydrophilicity of the resultant membranes; (ii) additional water transport channels due to the presence of O-MoS$_2$ and (iii) increased mean pore size of the composite HFUFMs after the addition of O-MoS$_2$, the increase of mean pore diameter is beneficial to the increase of permeation flux.

Nevertheless, the addition of over 0.20 wt.% O-MoS$_2$ would bring about a reduction in the permeability of the PMIA composite HFUFMs. With more than 0.20 wt.% O-MoS$_2$ content in the dope solution, its higher viscosity would slow the phase-inversion speed due to the lower diffusion of nonsolvent into the membranes, which would consequently reduce their pore size (Table 5). Furthermore, the reduction in porosity would then lead to the decrease in the PWFs of the membranes with more than 0.20 wt.% O-MoS$_2$ content.

3.4. Antifouling performance

Cyclic UF tests were performed on pure PMIA membranes and hybrid PMIA membranes to confirm the effects of O-MoS$_2$ nanosheets on fouling resistance. HA (500 ppm, pH = 6.8) and DI water were chosen as the model fouling
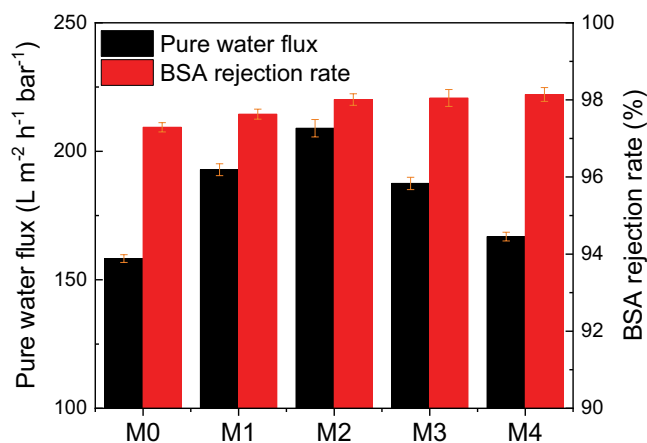
Fig. 8. Rejection rates and pure water flux of pristine PMIA and PMIA/O-MoS$_2$ HFUFMs (pH = 7.4, 1 bar).

Table 5
Detailed outer and inner diameter, pore size, membrane thickness, porosity and BSA rejection rates of the membranes

Membrane No.	OD (μm)	ID (μm)	δ (μm)	Mean pore size (nm)	ε (%)	BSA rejection (1,000 ppm) (%)
M0	1,200.0	650.0	275.0	6.5	81.3 ± 0.5	97.3
M1	1,270.0	670.0	300.0	7.9	80.7 ± 0.7	97.6
M2	1,150.0	590.0	280.0	7.8	80.3 ± 0.4	98.1
M3	1,240.0	670.0	285.0	7.1	79.7 ± 0.8	98.3
M4	1,360.0	720.0	320.0	7.0	76.0 ± 1.2	98.4

Note: OD: outer diameter, ID: inner diameter, δ: membrane thickness, ε: porosity.

agent and detergent, respectively, and the results are shown in Fig. 9.

As shown in Fig. 9a, during multicycle operations, the flux of the membranes decreased to 65%–75% in the first 1 h. After rinsed with DI water, the PWF recovered in different degrees instantly. Obviously, the PMIA/O-MoS$_2$ composite HFUFMs obtained higher flux recovery, indicating better antifouling properties than that of those pristine membranes.

Fig. 9b presents the FRR of each membrane in the 4th cyclic operation. The higher content of O-MoS$_2$ nanosheets modified UF membrane exhibited better FRR in HA solution. Compared with pristine membrane (FRR = 64.2%), the composite membrane with 0.3 wt.% of O-MoS$_2$ nanosheets blending showed excellent FRR up to 90.6% even after 4th cyclic operation. Fig. 9c quantified the fouling characteristics of pristine membrane and composite HFUFMs.
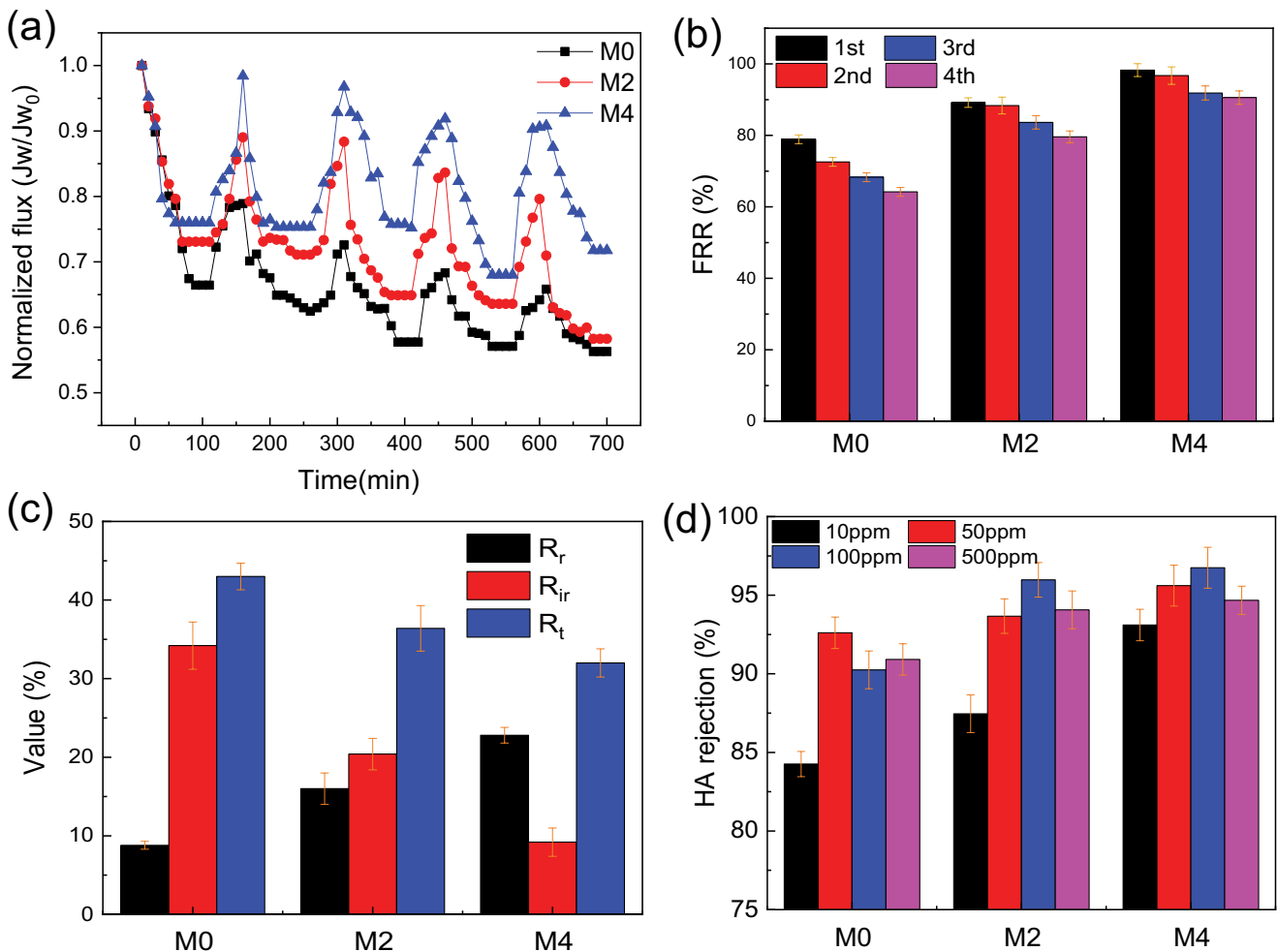
Fig. 9. (a) Normalized flux (J_W/J_{W0}), (b) flux recovery rate, (c) Rr (%), Rir (%) and Rt (%), of fabricated membranes after 10 h UF using 500 ppm HA solution (pH = 6.8, 1 bar) and (d) HA removal efficiency of pristine membrane and PMIA/O-MoS$_2$ composite membranes in solutions with HA concentration of 10, 50, 100 and 500 ppm, respectively. Tested at pressure of 1 bar.

Normally, fouling can be divided into reversible fouling (Rr) and irreversible fouling (Rir). Rr is usually caused by the weak interaction between pollutants and material surfaces, which could be recovered by physical washing. Conversely, the Rir resulted from the strong interactions between pollutants and interfacial surface, which could not be restored, and thus determined the total fouling (Rt). As shown in Fig. 9c, the composite HFUFMs showed the lowest Rir of 9.2% and Rt of 32.0% compared with that pristine membrane with Rir of 34.0% and Rt of 43.0%. It indicated that the modified membrane showed excellent antifouling characteristics. The improved antifouling capability of composite membrane is attributed to the enhanced membrane surface negative charge and hydrophilicity due to the incorporating of O-MoS$_2$ nanosheets. The HA molecules are assumed to be reversibly contacted with hydrophilic composite membrane

surface, which could be easily removed when washing with DI water. Besides, the enhanced static-electron repulsion interactions between negatively charged molecules and membrane surface hindered the deposition of HA on membrane surfaces. Fig. 10 depicts the antifouling behavior of the O-MoS$_2$ nanosheets modified composite membrane.

Finally, the separation performance of the prepared pristine membrane and composite HFUFMs in different concentrations of HA solution was examined. As shown in Fig. 9d, the rejection of HA for composite HFUFMs increased significantly compared with that of unmodified membrane. The higher concentration of O-MoS$_2$ leading to a better molecular rejection, which may have resulted from the steric effect between negatively charged HA (HA-) molecules (pH = 6.8) and similarly charged composite membrane [44]. The O-MoS$_2$ nanosheets modified composite HFUFMs
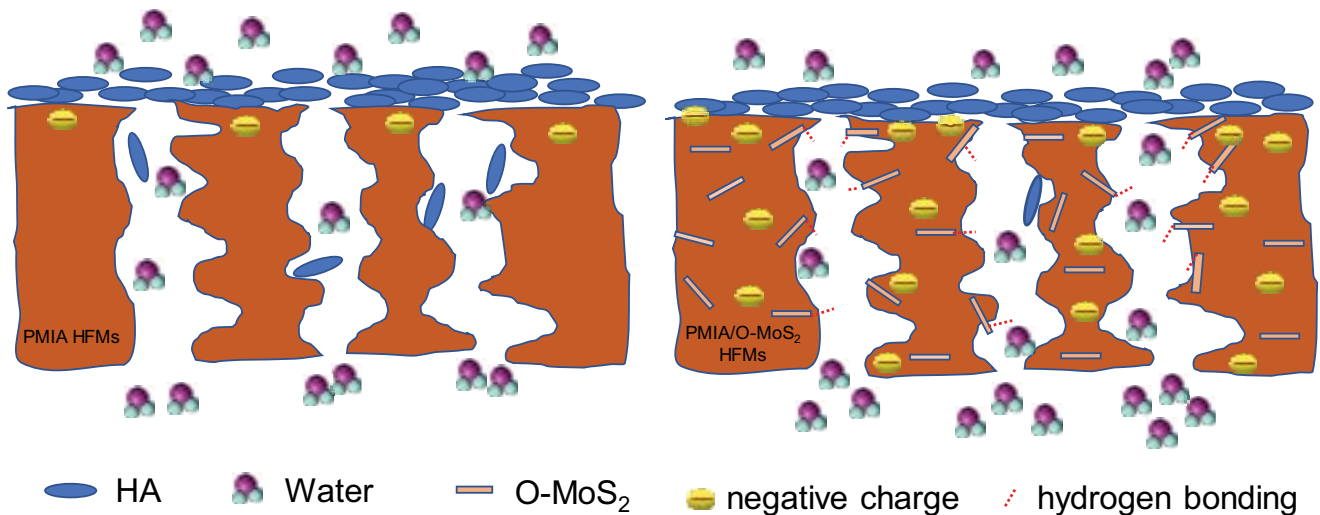
Fig. 10. Schematic illustration of the antifouling mechanisms of pristine PMIA and PMIA/O-MoS$_2$ HFUFMs.

Table 6
Comparison of the performance of the HFUFMs in the literature

Author	Hybrid membrane		Pure water flux (L m^{-2} h^{-1} bar^{-1})	Foulants	FRR	Year
Aditya Kiran et al. [46]	Original	17.5 PES/1 PAA	23.6	BSA	39.0	2016
	Modified	<1 GO	57.6		63.0	
Zhu et al. [47]	Original	22 PES/1 PVP	38.6	BSA	56.5	2016
	Modified	0.44 GO-PSBMA	71.7		96.4	
Xu et al. [48]	Original	15 PVDF/1PVP	158.1	BSA	43.1	2016
	Modified	1 GO/TiO$_2$	487.8		82.1	
Wu et al. [49]	Original	15 PVDF/1.5 F127	14.0	BSA/HA	57.5	2017
	Modified	≤0.5 GO-Ag	86.0		86.0	
Miao et al. [3]	Original	18 PVDF/3.0 PFSA	87.8	HA	50.7	2017
	Modified	≤0.5 SGO	174.2		90.1	
Saraswathi et al. [27]	Original	17.5 PEI/eMoS$_2$	12.6	HA	72.8	2018
	Modified	<2 eMoS$_2$	52.5		90.2	
This work	Original	14 PMIA/PEG	158.3	HA	64.2	
	Modified	≤0.3 O-MoS$_2$	209.0		90.6	

exhibited superior molecular rejection over 90% in different HA concentration. It demonstrated that the PMIA/O-MoS$_2$ composite HFUFMs have great promising application in micromolecular separation in aqueous solution. Table 6 shows the comparisons of the PMIA/O-MoS$_2$ composite HFUFMs performance with that of other modified membranes [3,27,46–49]. These results indicated that the PMIA/O-MoS$_2$ composite HFUFMs exhibited high improved pure water flux and FRR. As shown previously, the addition of O-MoS$_2$ nanosheets reconstructed the additional transmission channels of the composite membrane, improving the hydrophilicity, antifouling and changing the pore structure.

4. Conclusions

PMIA/O-MoS$_2$ composite HFUFMs with enhanced performance were successfully prepared through a dry-wet phase-inversion method. The high hydrophilicity of O-MoS$_2$ played a significant role in modifying the pore size, structure and antifouling ability of the hybrid membranes. With the addition of O-MoS$_2$, the contact angle of the PMIA hollow fiber UF membrane decreased from 72.9° to 55.3°, indicating that O-MoS$_2$ was directly related to the enhanced hydrophilic property of the PMIA hollow fiber composite membrane. The composite membrane with 0.20 wt.% O-MoS$_2$ showed the highest PWF (209.0 L m^{-2} h^{-1} bar^{-1}), which was 31.6 % higher than that of the original PMIA membrane (158.3 L m^{-2} h^{-1} bar^{-1}). Based on a comprehensive analysis of the pore size, pore structure, surface zeta potential and hydrophilicity of the membranes, the membrane composed of 0.20 wt.% O-MoS$_2$ has the highest water flux and antifouling ability. Considering their superior antifouling ability, excellent mechanical properties and high FRR, PMIA/O-MoS$_2$ composite HFUFMs are potential candidate materials as antifouling membranes in UF applications.

Acknowledgments

References

[1] H.J. Li, Y.M. Cao, L.Y. Yang, Q. Yuan, Oil-water separation performance of anti-fouling α-cellulose hollow fiber ultrafiltration membrane, Chem. J. Chinese U, 26 (2005) 1890–1895.

[2] J.G. Zhang, Z.W. Xu, W. Mai, C.Y. Min, B.M. Zhou, M.J. Shan, Y.L. Li, C.Y. Yang, Z. Wang, X.M. Qian, Improved hydrophilicity, permeability, antifouling and mechanical performance of PVDF composite ultrafiltration membranes tailored by oxidized low-dimensional carbon nanomaterials, J. Mater. Chem. A, 1 (2013) 3101–3111.

[3] W. Miao, Z.-K. Li, X. Yan, Y.-J. Guo, W.-Z. Lang, Improved ultrafiltration performance and chlorine resistance of PVDF hollow fiber membranes via doping with sulfonated graphene oxide, Chem. Eng. J., 317 (2017) 901–912.

[4] A.L. Ahmad, A.A. Abdulkarim, Z.M.H.M. Shafie, B.S. Ooi, Fouling evaluation of PES/ZnO mixed matrix hollow fiber membrane, Desalination, 403 (2017) 53–63.

[5] K. Parashuram, S.K. Maurya, H.H. Rana, P.S. Singh, P. Ray, A.V.R. Reddy, Tailoring the molecular weight cut off values of polyacrylonitrile based hollow fibre ultrafiltration membranes with improved fouling resistance by chemical modification, J. Membr. Sci., 425 (2013) 251–261.

[6] H.-P. Xu, W.-Z. Lang, X. Yan, X. Zhang, Y.-J. Guo, Preparation and characterizations of poly(vinylidene fluoride)/oxidized multi-wall carbon nanotube membranes with bi-continuous structure by thermally induced phase separation method, J. Membr. Sci., 467 (2014) 142–152.

[7] J. Huang, K.S. Zhang, The high flux poly (*m*-phenylene isophthalamide) nanofiltration membrane for dye purification and desalination, Desalination, 282 (2011) 19–26.

[8] T. Wang, C.W. Zhao, P. Li, Y. Li, J. Wang, Effect of non-solvent additives on the morphology and separation performance of poly(*m*-phenylene isophthalamide) (PMIA) hollow fiber nanofiltration membrane, Desalination, 365 (2015) 293–307.

[9] M. Yang, C.W. Zhao, S.F. Zhang, P. Li, D.Y. Hou, Preparation of graphene oxide modified poly(*m*-phenylene isophthalamide) nanofiltration membrane with improved water flux and antifouling property, Appl. Surf. Sci., 394 (2017) 149–159.

[10] M.X. Chen, C.F. Xiao, C. Wang, H.L. Liu, Studies on structure and properties of poly(*m*-phenylene isophthalamide) hollow fiber membranes, Acta Polym. Sin., 4 (2016) 428–435.

[11] Q.L. Jiang, K.S. Zhang, Preparation and characterization of high-flux poly(*m*-phenylene isophthalamide) (PMIA) hollow fiber ultrafiltration membrane, Desal. Wat. Treat, 138 (2019) 80–90.

[12] X. Wu, R.W. Field, J.J. Wu, K.S. Zhang, Polyvinylpyrrolidone modified graphene oxide as a modifier for thin film composite forward osmosis membranes, J. Membr. Sci., 540 (2017) 251–260.

[13] W. Zhang, W. Cheng, E. Ziemann, A. Be'er, X.L. Lu, M. Elimelech, R. Bernstein, Functionalization of ultrafiltration membrane with polyampholyte hydrogel and graphene oxide to achieve dual antifouling and antibacterial properties, J. Membr. Sci., 565 (2018) 293–302.

[14] S. Ayyaru, Y.-H. Ahn, Application of sulfonic acid group functionalized graphene oxide to improve hydrophilicity, permeability, and antifouling of PVDF nanocomposite ultrafiltration membranes, J. Membr. Sci., 525 (2017) 210–219.

[15] Q. Qin, Z.C. Hou, X.F. Lu, X.K. Bian, L.F. Chen, L.G. Shen, S. Wang, Microfiltration membranes prepared from poly (N-vinyl-2-pyrrolidone) grafted poly(vinylidene fluoride) synthesized by simultaneous irradiation, J. Membr. Sci., 427 (2013) 303–310.

[16] B.M. Ganesh, A.M. Isloor, A.F. Ismail, Enhanced hydrophilicity and salt rejection study of graphene oxide-polysulfone mixed matrix membrane, Desalination, 313 (2013) 199–207.

[17] J.D. Feng, M. Graf, K. Liu, D. Ovchinnikov, D. Dumcenco, M. Heiranian, V. Nandigana, N.R. Aluru, A. Kis, A. Radenovic, Single-layer MoS$_2$ nanopores as nanopower generators, Nature, 536 (2016) 197–200.

[18] L.W. Sun, H.B. Huang, X.S. Peng, Laminar MoS$_2$ membranes for molecule separation, Chem. Commun., 49 (2013) 10718–10720.

[19] Y. Li, S. Yang, K. Zhang, B. Van der Bruggen, Thin film nanocomposite reverse osmosis membrane modified by two dimensional laminar MoS$_2$ with improved desalination performance and fouling-resistant characteristics, Desalination, 454 (2019) 48–58.

[20] X. Liang, P. Wang, J. Wang, Y. Zhang, W. Wu, J. Liu, B. Van der Bruggen, Zwitterionic functionalized MoS$_2$ nanosheets for a novel composite membrane with effective salt/dye separation performance, J. Membr. Sci., 573 (2019) 270–279.

[21] Y.J. Wang, L.F. Liu, J.D. Hong, J. Cao, C.L. Deng, A novel Fe(OH)$_3$/g-C$_3$N$_4$ composite membrane for high efficiency water purification, J. Membr. Sci., 564 (2018) 372–381.

[22] R. Li, Y. Ren, P. Zhao, J. Wang, J. Liu, Y. Zhang, Graphitic carbon nitride (g-C$_3$N$_4$) nanosheets functionalized composite membrane with self-cleaning and antibacterial performance, J. Hazard. Mater., 365 (2019) 606–614.

[23] L.W. Sun, Y.L. Ying, H.B. Huang, Z.G. Song, Y.Y. Mao, Z.P. Xu, X.S. Peng, Ultrafast molecule separation through layered WS$_2$ nanosheet membranes, ACS Nano, 8 (2014) 6304–6311.

[24] W.W. Lei, D. Portehault, D. Liu, S. Qin, Y. Chen, Porous boron nitride nanosheets for effective water cleaning, Nat. Commun., 4 (2013) 1777.

[25] X.B. Fan, P.T. Xu, D.K. Zhou, Y.F. Sun, Y.G.C. Li, M.A.T. Nguyen, M. Terrones, T.E. Mallouk, Fast and efficient preparation of exfoliated 2H MoS$_2$ nanosheets by sonication-assisted lithium intercalation and infrared laser-induced 1T to 2H phase reversion, Nano Lett., 15 (2015) 5956–5960.

[26] E. Singh, K.S. Kim, G.Y. Yeom, H.S. Nalwa, Atomically thin-layered molybdenum disulfide (MoS$_2$) for bulk-heterojunction solar cells, ACS Appl. Mater. Interfaces, 9 (2017) 3223–3245.

[27] M.S.S.A. Saraswathi, D. Rana, A. Nagendran, S. Alwarappan, Custom-made PEI/exfoliated-MoS$_2$ nanocomposite ultrafiltration membranes for separation of bovine serum albumin and humic acid, Mater. Sci. Eng., C, 83 (2018) 108–114.

[28] F.S. Pan, H. Ding, W.D. Li, Y.M. Song, H. Yang, H. Wu, Z.Y. Jiang, B.Y. Wang, X.Z. Cao, Constructing facilitated transport pathway in hybrid membranes by incorporating MoS2 nanosheets, J. Membr. Sci., 545 (2018) 29–37.

[29] A. Gogoi, T.J. Konch, K. Raidongia, K.A. Reddy, Water and salt dynamics in multilayer graphene oxide (GO) membrane: role of lateral sheet dimensions, J. Membr. Sci., 563 (2018) 785–793.

[30] M. Amini, S.A.A. Ramazani, M. Faghihi, S. Fattahpour, Preparation of nanostructured and nanosheets of MoS$_2$ oxide using oxidation method, Ultrason. Sonochem., 39 (2017) 188–196.

[31] H.L. Liu, C.F. Xiao, X.Y. Hu, M.T. Liu, Post-treatment effect on morphology and performance of polyurethane-based hollow fiber membranes through melt-spinning method, J. Membr. Sci., 427 (2013) 326–335.

[32] R.I. Peinador, J.I. Calvo, P. Prádanos, L. Palacio, A. Hernández, Characterisation of polymeric UF membranes by liquid–liquid displacement porosimetry, J. Membr. Sci., 348 (2010) 238–244.

[33] Q. Yang, T.-S. Chung, Y.E. Santoso, Tailoring pore size and pore size distribution of kidney dialysis hollow fiber membranes via dual-bath coagulation approach, J. Membr. Sci., 290 (2007) 153–163.

[34] J.I. Calvo, A. Bottino, G. Capannelli, A. Hernández, Pore size distribution of ceramic UF membranes by liquid–liquid displacement porosimetry, J. Membr. Sci., 310 (2008) 531–538.

[35] L.-Y. Yu, Z.-L. Xu, H.-M. Shen, H. Yang, Preparation and characterization of PVDF–SiO$_2$ composite hollow fiber UF membrane by sol–gel method, J. Membr. Sci., 337 (2009) 257–265.

[36] H. Li, Q. Zhang, C.C.R. Yap, B.K. Tay, T.H.T. Edwin, A. Olivier, D. Baillargeat, From bulk to monolayer MoS$_2$: evolution of Raman scattering, Adv. Funct. Mater., 22 (2012) 1385–1390.

[37] C. Lee, H. Yan, L.E. Brus, T.F. Heinz, J. Hone, S. Ryu, Anomalous lattice vibrations of single- and few-layer MoS$_2$, ACS Nano, 4 (2010) 2695–2700.

[38] D. Gopalakrishnan, D. Damien, M.M. Shaijumon, MoS$_2$ quantum dot-interspersed exfoliated MoS$_2$ nanosheets, ACS Nano, 8 (2014) 5297–5303.

[39] L. Yan, Y.S. Li, C.B. Xiang, S. Xianda, Effect of nano-sized Al$_2$O$_3$-particle addition on PVDF ultrafiltration membrane performance, J. Membr. Sci., 276 (2006) 162–167.

[40] A. Khan, T.A. Sherazi, Y. Khan, S.H. Li, S.A.R. Naqvi, Z.L. Cui, Fabrication and characterization of polysulfone/ modified nanocarbon black composite antifouling ultrafiltration membranes, J. Membr. Sci., 554 (2018) 71–82.

[41] C.-E. Lin, J. Wang, M.-Y. Zhou, B.-K. Zhu, L.-P. Zhu, C.-J. Gao, Poly(m-phenylene isophthalamide) (PMIA): a potential polymer for breaking through the selectivity-permeability trade-off for ultrafiltration membranes, J. Membr. Sci., 518 (2016) 72–78.

[42] D. Voiry, M. Salehi, R. Silva, T. Fujita, M.W. Chen, T. Asefa, V.B. Shenoy, G. Eda, M. Chhowalla, Conducting MoS$_2$ nanosheets as catalysts for hydrogen evolution reaction, Nano Lett., 13 (2013) 6222–6227.

[43] S. Singh, K.C. Khulbe, T. Matsuura, P. Ramamurthy, Membrane characterization by solute transport and atomic force microscopy, J. Membr. Sci., 142 (1998) 111–127.

[44] I.H. Alsohaimi, M. Kumar, M.S. Algamdi, M.A. Khan, K. Nolan, J. Lawler, Antifouling hybrid ultrafiltration membranes with high selectivity fabricated from polysulfone and sulfonic acid functionalized TiO$_2$ nanotubes, Chem. Eng. J., 316 (2017) 573–583.

[45] Z.H. Wang, H.R. Yu, J.F. Xia, F.F. Zhang, F. Li, Y.Z. Xia, Y.H. Li, Novel GO-blended PVDF ultrafiltration membranes, Desalination, 299 (2012) 50–54.

[46] S. Aditya Kiran, Y. Lukka Thuyavan, G. Arthanareeswaran, T. Matsuura, A.F. Ismail, Impact of graphene oxide embedded polyethersulfone membranes for the effective treatment of distillery effluent, Chem. Eng. J., 286 (2016) 528–537.

[47] J. Zhu, M. Tian, J. Hou, J. Wang, J. Lin, Y. Zhang, J. Liu, B. Van der Bruggen, Surface zwitterionic functionalized graphene oxide for a novel loose nanofiltration membrane, J. Mater. Chem. A, 4 (2016) 1980–1990.

[48] Z. Xu, T. Wu, J. Shi, K. Teng, W. Wang, M. Ma, J. Li, X. Qian, C. Li, J. Fan, Photocatalytic antifouling PVDF ultrafiltration membranes based on synergy of graphene oxide and TiO$_2$ for water treatment, J. Membr. Sci., 520 (2016) 281–293.

[49] Q. Wu, G.-E. Chen, W.-G. Sun, Z.-L. Xu, Y.-F. Kong, X.-P. Zheng, S.-J. Xu, Bio-inspired GO-Ag/PVDF/F127 membrane with improved anti-fouling for natural organic matter (NOM) resistance, Chem. Eng. J., 313 (2017) 450–460.